Title

Electric field manipulation of spin chirality and skyrmion dynamic.

Journal

Science Advances, 9(7)

Authors

Dai, Bingqian
Wu, Di
Razavi, Seyed
et al.

Publication Date

2023-02-15

DOI

10.1126/sciadv.ade6836

PHYSICAL SCIENCES

Electric field manipulation of spin chirality and skyrmion dynamic

Bingqian Dai[1]*, Di Wu[1], Seyed Armin Razavi[1], Shijie Xu[1], Haoran He[1], Qingyuan Shu[1], Malcolm Jackson[1], Farzad Mahfouzi[2], Hanshen Huang[1], Quanjun Pan[1], Yang Cheng[1], Tao Qu[1], Tianyi Wang[1], Lixuan Tai[1], Kin Wong[1], Nicholas Kioussis[2], Kang L. Wang[1]*

The Dzyaloshinskii-Moriya interaction (DMI) is an antisymmetric exchange interaction that stabilizes spin chirality. One scientific and technological challenge is understanding and controlling the interaction between spin chirality and electric field. In this study, we investigate an unconventional electric field effect on interfacial DMI, skyrmion helicity, and skyrmion dynamics in a system with broken inversion symmetry. We design heterostructures with a 3d-5d atomic orbital interface to demonstrate the gate bias control of the DMI energy and thus transform the DMI between opposite chiralities. Furthermore, we use this voltage-controlled DMI (VCDMI) to manipulate the skyrmion spin texture. As a result, a type of intermediate skyrmion with a unique helicity is created, and its motion can be controlled and made to go straight. Our work shows the effective control of spin chirality, skyrmion helicity, and skyrmion dynamics by VCDMI. It promotes the emerging field of voltage-controlled chiral interactions and voltage-controlled skyrmionics.

INTRODUCTION

Chirality is an asymmetric structural property for which an object cannot be mapped onto its mirror image, giving rise to a handedness. It is a fundamental feature that governs many essential properties in nature. In magnetic materials, inversion symmetry breaking can give rise to chirality in exchange coupling known as Dzyaloshinskii-Moriya interaction (DMI) (*1*, *2*), whose Hamiltonian is defined for neighboring atomic spins $\boldsymbol{S}_{i,j}$ as: $H_{\mathrm{DMI}} = -\mathbf{D}_{ij} \bullet (\boldsymbol{S}_i \times \boldsymbol{S}_j)$ (*1*, *2*), where $\mathbf{D}_{ij}$ denotes the DMI vector. Bulk DMI arises from limited bulk materials with inversion asymmetry in crystal (*3*–*5*). Interfacial DMI (iDMI) (*6*, *7*) arises from the interface of, e.g., a heavy metal/thin-film ferromagnet (HM/FM) (*8*) heterostructure with strong spin-orbit coupling. The iDMI stabilizes chiral topological spin textures, e.g., skyrmion and domain wall (DW) (*9*–*12*). The topological degree of freedom gives rise to abundant physics, such as the emergent electromagnetic field and the skyrmion Hall effect. Skyrmion/DW can also be exploited as a solitonic information carrier that could be created, deleted, and shifted electrically (*13*–*15*), and thus, the understanding and control of their motion become extremely important. The characteristics of skyrmion/DW depend intimately on the iDMI. For instance, the handedness of homochiral DW/skyrmion is determined by the sign of iDMI (*12*, *16*, *17*), and the relativistic solitonic motion, topological stability, and minimum size of DW/skyrmion can vary by orders of magnitude depending on the iDMI strength (*18*–*22*). Therefore, insightful understanding and effective control of iDMI have substantial scientific and technological ramifications. Recent progress in controlling iDMI has been made by exploring different stackings of various HM/FM heterostructures (*6*, *7*). The effective tuning of iDMI has also been achieved by introducing ionic species such as oxygen and hydrogen via chemisorption (*23*, *24*).

The effect of electric field on DMI and their atomic-scale understanding have rarely been explored. Only a limited number of pioneering works (*25*, *26*) have demonstrated the effect of voltage-controlled DMI (VCDMI), and they focused only on tuning iDMI strength in a fixed chirality region. Furthermore, the use of the electric field or voltage would offer a more functional device platform that is vital for low-energy and high-speed operations (*27*–*29*). It would also provide a unique opportunity to manipulate the skyrmion topology and helicity and investigate the topology- and helicity-dependent skyrmion physics, such as the skyrmion Hall effect. Moreover, if both the chirality and strength of iDMI can be controlled electrically to affect the motion of a homochiral skyrmion, then it would resolve today's critical challenge in controlling the skyrmion motion.

Here, we provide a physical understanding of the electric field interaction with iDMI in a heterostructure and demonstrate two experimental results. First, we show that by applying a gate bias to the Ta/CoFeB/Ir/MgO heterostructures, the electric field on the 3d-5d orbitals at the CoFeB-Ir interface can drive the transition of the iDMI chirality and manipulate the iDMI strength. In particular, we show that the iDMI energy can be changed from −100 to +12 μJ/m^2 with a VCDMI coefficient ($\xi \equiv \Delta_{\mathrm{iDMI}}/\Delta_{E\ -\ \mathrm{field}}$) of ξ = +130 fJ/Vm. Second, we use this VCDMI effect to investigate its effect on a homochiral skyrmion and show that the skyrmion Hall angle can be controlled electrically by the skyrmion's helicity. As a result, we can create a type of intermediate skyrmion with a unique helicity such that this intermediate skyrmion can be manipulated to move straight forward with a near-zero skyrmion Hall angle. Our work provides a platform for investigating chiral interactions and shows the manipulation of skyrmions for low-power spintronics by voltage instead of electric current.

[1]Departments of Electrical and Computer Engineering, Physics and Astronomy, and Material Science and Engineering, University of California, Los Angeles, Los Angeles, CA 90095, USA. [2]Department of Physics and Astronomy, California State University, Northridge, Los Angeles, CA 91330-8268, USA.
*Corresponding author. Email: bdai@g.ucla.edu (B.D.); wang@ee.ucla.edu (K.L.W.)

RESULTS

Iridium interface structure for VCDMI

Studies (*6*–*8*) have revealed that the sign and magnitude of the iDMI vector ($\mathbf{D}_{ij}$) are determined by the interfacial electronic structure of the HM/FM interface, and both Ta/CoFeB and Ir/CoFeB structures were shown to have positive iDMI (*6*). According to Fert and Levy (*8*), an inverted stacking of CoFeB/Ir could give a negative iDMI. As illustrated in Fig. 1A, the direction of $\mathbf{D}_{ij}$ is given by $\mathbf{r}_1 \times \mathbf{r}_2$, where $\mathbf{r}$ is the position vector pointing from the HM atom (Ir and Ta) to the FM atom (CoFeB). As a result, the top Ir surface has a negative (counterclockwise) Ir DMI or $\mathbf{D}_{\mathrm{Ir}}$, pointing out of the paper. The bottom Ta surface has a positive (clockwise) Ta DMI or $\mathbf{D}_{\mathrm{Ta}}$, pointing into the paper. Therefore, from these, we conceive and design a hetero-stack consisting of Ta/CoFeB/Ir/MgO heterostructures, with two iDMIs ($\mathbf{D}_{\mathrm{Ta}}$ and $\mathbf{D}_{\mathrm{Ir}}$) of opposite signs, exhibiting a competing net iDMI. If the net iDMI ($\mathbf{D}_i$) or chirality is negative, the spins rotate counterclockwise; the positive $\mathbf{D}_i$ gives rise to clockwise spin rotation.

If the net iDMI of the system could be tuned to zero, then this singular point would provide opportunities to study critical phenomena such as the DMI chirality transition and its effects on chiral topological solitons such as skyrmion and DW. Hence, we construct the [Ta(5)/CoFeB(0.9)/Ir(0.03 to 0.15)/MgO(2)/Al_2O_3(5)] heterostructures, with a nominal thickness in nanometers, in which the Ir thickness variation is achieved through a wedged structure (see Materials and Methods). The Ir layer is designed to have a smooth varying thickness to induce a gradual change in iDMI across the wafer. The measured net iDMI, $\mathbf{D}_i$, as shown in Fig. 1B, shows a monotonical decrease from +135 to −45 μJ/m^2 as the Ir thickness (t_{Ir}) increases from 0 to 0.15 nm (the $\mathbf{D}_i$ measurement technique will be discussed in the next paragraph). In particular, the small $\mathbf{D}_i$ region (+68 to −45 μJ/m^2) is found between t_{Ir} values of 0.09 and 0.15 nm, with 0.12 nm giving rise to zero-$\mathbf{D}_i$. The electric field–driven DMI chirality transition, as well as its effect on homochiral skyrmion and DW, is investigated in this thickness range and will be discussed in the following sections. We note that Fig. 1B displays two linear $\mathbf{D}_i$ regions with different slopes as a function of Ir thickness. This difference is possibly due to the discontinuous Ir layer, i.e., some Ir atoms form discontinuous islands when the nominal thickness t_{Ir} is too thin as in the first segment when $t_{\mathrm{Ir}} \leq 0.06$ nm. However, when Ir becomes thicker, the layer becomes comparatively more continuous, and the slope maintains constant for $t_{\mathrm{Ir}} > 0.06$ nm. First-principles calculations are presented in fig. S1 to support our experimental result and give further insights into the atomistic understanding of iDMI.

$\mathbf{D}_i$ is measured using a slightly modified approach based on the well-established spin Hall torque magnetometry (*30*, *31*), using the spin-orbit torque (SOT)–driven DW motion to quantify the $\mathbf{D}_i$ sign and strength. The snapshots of DW motion and the measurement setup are illustrated in Fig. 1C. The [Ta (5)/CoFeB (0.9)/Ir (0.03 to 0.15)/MgO (2)/Al_2O_3 (5)] multilayers (thickness in nanometers) are patterned into a DW racetrack-like strip structure. A down-up

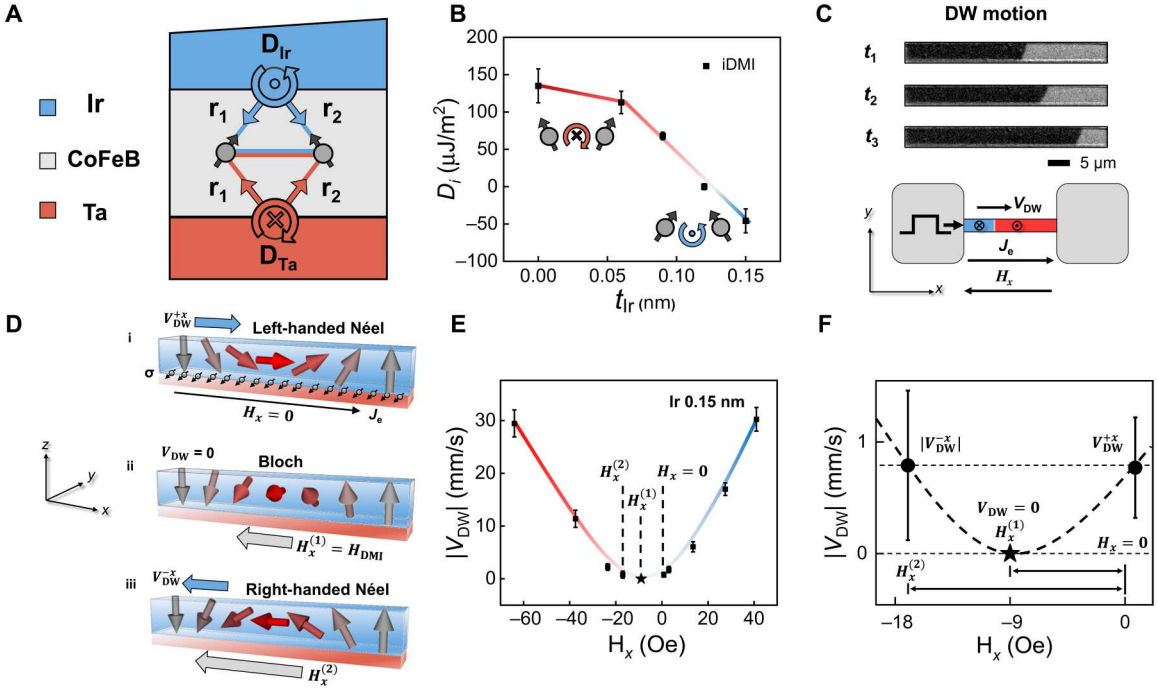

Fig. 1. Ir interface structure for studying VCDMI. (**A**) Material stack of Ta/CoFeB/Ir wedge. The gray circle with a black arrow denotes the FM atom. The blue and red straight arrows represent the position vectors $\mathbf{r}_1$ and $\mathbf{r}_2$. The blue and red circular arrows denote the Ir and Ta atom and their iDMI vector direction (chirality). The iDMI from Ta/CoFeB ($\mathbf{D}_{\mathrm{Ta}}$) and CoFeB/Ir ($\mathbf{D}_{\mathrm{Ir}}$) interfaces are of opposite signs. (**B**) $\mathbf{D}_i$ versus Ir layer thickness (t_{Ir}). Color code: Red accounts for positive $\mathbf{D}_i$ values, white represents zero $\mathbf{D}_i$, and blue denotes negative $\mathbf{D}_i$. (**C**) Snapshots of SOT-driven DW motion. Illustration of the experimental setup: DW motion device, SOT-driven down-up DW motion under $\boldsymbol{H_x}$ and $\boldsymbol{J_e}$. (**D**) DW spin configuration and DW motion under $\boldsymbol{H_x}$ (**−*x*** direction), $\boldsymbol{J_e}$ (**+*x*** direction), and σ (**−*y*** direction). (i) $\boldsymbol{H_x} = 0$, the DW is a left-handed Néel type with a **+*x***-direction velocity $\boldsymbol{V}_{\mathrm{DW}}^{+x}(\boldsymbol{H_x} = 0)$. (ii) $\boldsymbol{H}_x^{(1)}$ is applied. The DW changes to Bloch type and stops its motion, $\boldsymbol{V}_{\mathrm{DW}}[\boldsymbol{H}_x^{(1)}] = 0$. (iii) $\boldsymbol{H_x}$ is increased to $\boldsymbol{H}_x^{(2)}$. The DW changes to a right-handed Néel type with a **−*x***-direction velocity $\boldsymbol{V}_{\mathrm{DW}}^{-x}[\boldsymbol{H}_x^{(2)}]$; $\boldsymbol{V}_{\mathrm{DW}}^{-x} = -\boldsymbol{V}_{\mathrm{DW}}^{+x}$. (**E**) The full-range $|\boldsymbol{V}_{\mathrm{DW}}|$ versus $\boldsymbol{H_x}$ plot. (**F**) Zoom-in plot of (E) near $\boldsymbol{V}_{\mathrm{DW}} = 0$ to show the $[\boldsymbol{H}_x^{(1)}, \boldsymbol{V}_{\mathrm{DW}} = 0]$, $[\boldsymbol{H}_x^{(1)}, \boldsymbol{V}_{\mathrm{DW}} = 0]$, and $[\boldsymbol{H}_x^{(2)}, \boldsymbol{V}_{\mathrm{DW}}^{-x}]$ data.

($-M_Z$, DW, $+M_Z$) DW is nucleated on the left side of the device. As illustrated in Fig. 1D (i), when a $+\boldsymbol{x}$-direction electron current $\boldsymbol{J_e}$ is applied through the Ta underlayer, the spin Hall effect from the Ta generates a spin accumulation $\sigma \sim -\hat{\boldsymbol{z}} \times \boldsymbol{J_e} \sim -\hat{\boldsymbol{y}}$ at the Ta/CoFeB interface (σ is illustrated as the small black spins at the interface) (*9*, *13*, *32*). The σ creates a damping-like torque and drives the DW motion (*9*–*13*).

We next discuss the three steps to get the parameters for calculating the $\mathbf{D}_i$ value. In Fig. 1D (i), no external magnetic field is applied ($\boldsymbol{H_x} = 0$), the DW is a left-handed Néel type (counterclockwise rotation), and we get a $+\boldsymbol{x}$-direction velocity $\boldsymbol{V}_{\mathrm{DW}}^{+\boldsymbol{x}}[\boldsymbol{H_x} = 0]$. In Fig. 1D (ii), an external magnetic field $\boldsymbol{H}_{\boldsymbol{x}}^{(1)}$ in the $-\boldsymbol{x}$ direction is applied to counteract the DMI effective field $\boldsymbol{H_{DMI}}$ to alter the DW spin configuration. If $\boldsymbol{H}_{\boldsymbol{x}}^{(1)}$ is large enough to precisely compensate $\boldsymbol{H_{DMI}}$, then the DW changes to Bloch type and stops its motion, $\boldsymbol{V}_{\mathrm{DW}}[\boldsymbol{H}_{\boldsymbol{x}}^{(1)}] = 0$. In Fig. 1D (iii), the field is further increased to $\boldsymbol{H}_{\boldsymbol{x}}^{(2)}$. The DW changes to a right-handed Néel type (clockwise rotation) with a $-\boldsymbol{x}$-direction velocity $\boldsymbol{V}_{\mathrm{DW}}^{-\boldsymbol{x}}[\boldsymbol{H}_{\boldsymbol{x}}^{(2)}]$; here, $\boldsymbol{V}_{\mathrm{DW}}^{-\boldsymbol{x}}[\boldsymbol{H}_{\boldsymbol{x}}^{(2)}] = -\boldsymbol{V}_{\mathrm{DW}}^{+\boldsymbol{x}}[\boldsymbol{H_x} = 0]$, i.e., they have the same magnitude but with an opposite sign. The full-range $|\boldsymbol{V_{DW}}|$ versus $\boldsymbol{H_x}$ plot is shown in Fig. 1E. The $[\boldsymbol{H_x} = 0, \boldsymbol{V}_{\mathrm{DW}}^{+\boldsymbol{x}}]$, $[\boldsymbol{H}_{\boldsymbol{x}}^{(1)}, \boldsymbol{V}_{\mathrm{DW}} = 0]$, and $[\boldsymbol{H}_{\boldsymbol{x}}^{(2)}, \boldsymbol{V}_{\mathrm{DW}}^{-\boldsymbol{x}}]$ in the zoom-in plot near $\boldsymbol{V_{DW}} \approx 0$ is shown in Fig. 1F. The DMI effective field $\boldsymbol{H_{DMI}}$ and DW shape anisotropy field $\boldsymbol{H_{DW}}$ can be obtained respectively from (*30*, *31*) $\boldsymbol{H}_{\mathrm{DMI}} = \boldsymbol{H}_{\boldsymbol{x}}^{(1)} = 9$ Oe and $\frac{2}{\pi}\boldsymbol{H}_{\mathrm{DW}} = \boldsymbol{H}_{\boldsymbol{x}}^{(2)} - \boldsymbol{H}_{\boldsymbol{x}}^{(1)} = 8$ Oe; the $\mathbf{D}_i$ constant is then calculated as (*30*, *31*): $D_i = \mu_0 H_{\mathrm{DMI}} M_s \Delta$, and $\Delta = \frac{M_s t \ln(2)}{\pi H_{\mathrm{DW}}}$, where μ_0 is the vacuum permeability, M_s is the saturation magnetization (whose measurement is shown in fig. S2), Δ is the DW width (*30*, *31*), and $t = 0.9$ nm is the CoFeB thickness. From these data, we find $D_i \approx -64.3$ μJ/m^2 at $t_{\mathrm{Ir}} = 0.15$ nm for this device. The detailed measurement mechanism and velocity tracking technique are discussed in figs. S3 and S4, respectively.

Voltage control of the chirality and strength of iDMI

Previous theoretical studies (*33*, *34*) reveal that the chirality and magnitude of the iDMI are closely associated with the band filling and hybridization between, e.g., 3d and 5d orbitals near the Fermi level. Thus, even a tiny shift of the Fermi level could substantially change the iDMI energy (*33*, *34*). Our multilayer stack Ta/CoFeB/Ir/MgO provides an ideal platform for investigating the effect of electric field on DMI and the critical DMI chirality transition as well as on homochiral DW/skyrmion. The thin subnanometer Ir ensures a strong electric field at the CoFeB/Ir interface despite the metal's finite Coulomb screening length (few angstroms) (*35*). As a result, substantial electron accumulation or depletion, resulting in a shift of the Fermi level at the CoFeB/Ir interface, will alter the electronic structures and thus drive the DMI chirality transition.

In the experiment, the electric field is applied to the CoFeB/Ir surface through a MgO dielectric layer, as illustrated in Fig. 2A (left). The experimental setup is shown on the right of Fig. 2A. In this case, the top gate is a transparent electrode (see Materials and Methods) to observe the DW motion. We apply a top-gate voltage (V_G) to the DW motion device and measure the resulting $\mathbf{D}_i$ using the same method discussed in the previous section. The measured VCDMI of two representative Ir thicknesses is shown in Fig. 2B. The data show two distinct slopes for the two Ir thicknesses: For t_{Ir}=0.15 nm, the $\mathbf{D}_i$ changes from −100 to +12 μJ/m^2 with a VCDMI coefficient ξ ($\xi \equiv \Delta_{\mathrm{iDMI}}/\Delta_{E\ -\ \mathrm{field}}$) of ξ = 130 fJ/Vm, and for t_{Ir}=0.06 nm, ξ = 25 fJ/Vm. The ξ (the slope) is observed to increase with t_{Ir}, possibly because, again, the Ir atoms form a complete layer as the thickness increases, giving a stronger effect of electric field on DMI and thus a larger ξ, consistent with Fig. 1B. The voltage-driven $\mathbf{D}_i$ chirality transition occurs at t_{Ir} = 0.15 nm. When $V_G < +25$ V, the $\mathbf{D}_i$ remains negative, and at $V_G = +25$ V (E field ≈ 0.3 V/nm), $\mathbf{D}_i$ becomes zero. Here, we define $V_0 = +25$ V as the critical voltage for zero iDMI energy, which is also the critical point that separates the opposite chiralities. As V_G increases to +35 V (E field ≈ 0.4 V/nm), $\mathbf{D}_i$ changes sign and becomes positive. Although this VCDMI effect takes place at the atomic scale, its effect on mesoscopic homochiral DW can be directly observed from the DW motion. The DW spin profile and snapshots of SOT-driven DW motion under gate bias for this t_{Ir} = 0.15 nm are shown in Fig. 2C. When $V_G < V_0$, the SOT current drives the down-up DW to move in the $+\boldsymbol{x}$ direction, which indicates that the DW is a left-handed Néel type (counterclockwise rotation with a negative $\mathbf{D}_i$). At $V_G = V_0$ (+25 V), the DW motion stops, indicating that the DW transforms into a Bloch type (a zero $\mathbf{D}_i$). Further increase in V_G to +35 V ($V_G > V_0$), the DW propagation direction is reversed to the $-\boldsymbol{x}$ direction because the DW becomes a right-handed Néel type (clockwise rotation with a positive $\mathbf{D}_i$). These observations confirm the iDMI chirality transition and reveal the interplay between electronic structure and spin chirality as well as its impact on mesoscopic spin textures. Micromagnetic simulations of DW motion are presented in fig. S5 to corroborate the above findings. To further confirm that this DMI–electric field effect comes from the 3d-5d CoFeB/Ir interface, we perform a control experiment for the stack without Ir insertion, Ta/CoFeB/MgO. The results (Fig. 2D) show no obvious change in $\mathbf{D}_i$. The data of the control device only show a small drop of the $\mathbf{D}_i$ value at the highest positive V_G. However, this change is opposite to the positive VCDMI slope as shown for the Ir device (Fig. 2B). We speculate that this effect might come from the CoFeB/MgO interface, suggesting that the DMI–electric field coupling could also arise between 3d FM and 2p light elements such as oxygen. However, it needs further experimental and theoretical efforts to confirm this speculation, which is beyond the scope of this work. Last, we perform electric transport measurements shown in fig. S6 to rule out other effects affecting the $\mathbf{D}_i$, such as voltage-induced change of M_s.

Manipulation of the skyrmion motion

Having established the VCDMI, we next use this effect to investigate its impact on the spin textures of homochiral skyrmions and the helicity-dependent skyrmion Hall effect (*36*–*38*). DW and skyrmion are two different types of topological excitations: As shown in previous sections, DW can be described by a one-dimensional (1D) spin chain in which the spins can be mapped onto a unit circle, while skyrmion is a 2D soliton whose spins can be mapped onto a unit sphere. This extra degree of freedom gives rise to more complex skyrmion dynamics, such as the skyrmion Hall effect (*36*–*38*). The skyrmion Hall effect is manifested as a topology-induced transverse velocity acquired by the current-driven skyrmions, analogous to the conventional Hall effect from the motion of a charged particle (*36*–*38*). As a result, the skyrmions traverse with a skyrmion Hall angle θ_{SKH} relative to the current direction (in oblique motion), as illustrated in Fig. 3A (i). Unlike the DW motion, which is confined along the current direction, Bloch and Néel skyrmions tend to

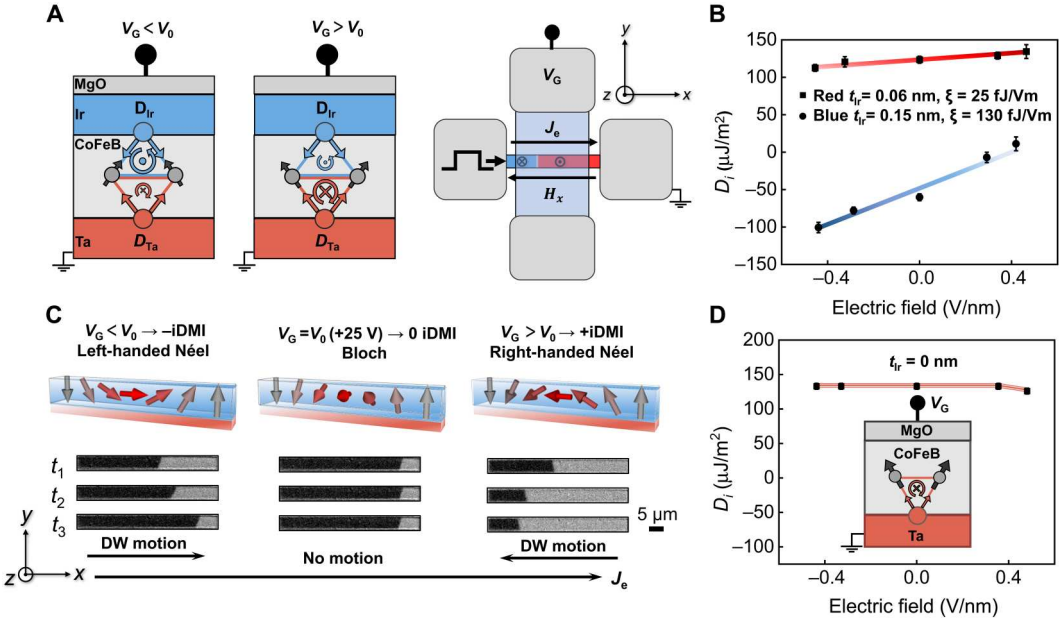

Fig. 2. Voltage control of iDMI chirality and strength. (**A**) Left: Ta/CoFeB/Ir/MgO heterostructures with an applied bias V_G. The $\mathbf{D}_i$'s chirality is left-handed when $V_G < V_0$ and becomes right-handed when $V_G > V_0$. The larger-size blue and red circular arrows indicate the dominant chirality for these two V_G cases. Right: Measurement setup. The blue transparent strip denotes the top-gate electrode. (**B**) $\mathbf{D}_i$ versus electric field plot for Ir thicknesses of 0.06 and 0.15 nm. For t_{Ir} = 0.15 nm, the $\mathbf{D}_i$ becomes zero when $V_G = V_0$ = +25 V (*E* field, ~0.3 V/nm). The $\mathbf{D}_i$ changes to +12 μJ/m² when V_G = +35 V > V_0 (*E* field, ~0.4 V/nm). (**C**) DW spin configurations and snapshots of DW motion under different V_G values for t_{Ir} = 0.15 nm. $\boldsymbol{J_e}$ is in the **+*x*** direction. When $V_G < V_0$, the DW moves to the right (i.e., $-\mathbf{D}_i$, left-handed Néel). When $V_G = V_0$, the DW motion stops, indicating a vanishing $\mathbf{D}_i$ (Bloch). When V_G = +35 V > V_0, the DW motion direction reverses to the left ($+\mathbf{D}_i$, right-handed Néel). (**D**) Control experiment of VCDMI in a Ta/CoFeB/MgO stack without Ir insertion. The $\mathbf{D}_i$ shows negligible changes besides the data point at the highest positive electric field.

move orthogonally to each other (*36*), forming opposite skyrmion Hall angles, as illustrated in Fig. 3A (i). Theoretically, the skyrmion Hall angle θ_{SKH} can be obtained from the solution of the Thiele equation for a skyrmion with a given helicity or spin rotation angle ψ (*36*–*38*): $\theta_{SKH} = \tan^{-1}\left(\frac{G\cos\psi - \alpha D_{xx}\sin\psi}{G\sin\psi + \alpha D_{xx}\cos\psi}\right)$, where $G = -4\pi N_{sk}$ is the gyrotropic factor and $N_{sk} = \pm 1$ is the skyrmion winding number, D_{xx} is the diagonal of the isotropic dissipation tensor, and α is the Gilbert damping. As illustrated in Fig. 3A (ii), the helicity or spin rotation angle ψ follows a spherical symmetry. For a Néel skyrmion, ψ = 0 or π, and for a Bloch skyrmion, $\psi = \frac{\pi}{2}$ or $\frac{3\pi}{2}$. Hence, by driving the transition between skyrmion types and thus tuning ψ, a critical ψ can be found to make the skyrmion Hall angle vanish $\theta_{SKH} = 0$.

Therefore, if we could continuously deform a Néel skyrmion to Bloch type, we might find a superposition or an intermediate state of those two types of skyrmions. This "intermediate" skyrmion has zero θ_{SKH} and could move straight forward along the current direction, as illustrated in Fig. 3A (i). The three types of skyrmions in Fig. 3A are created by micromagnetic simulation using the MuMax3 software (*39*), and our simulation shows that the transition between skyrmion types depends intimately on the iDMI magnitude: The Néel skyrmion transforms into an intermediate skyrmion when the $\mathbf{D}_i$ is decreased from 500 to 200 μJ/m², and the intermediate skyrmion transforms into a Bloch skyrmion when $\mathbf{D}_i$ is below 50 μJ/m². These $\mathbf{D}_i$ magnitudes are obtained from the simulation at T = 0 K. As can be seen in the magnified skyrmion spin texture in Fig. 3A (ii), the ψ of an intermediate skyrmion is clearly in between the Néel and Bloch types.

As demonstrated in earlier sections, $\mathbf{D}_i$ of the Ta/CoFeB/Ir/MgO heterostructures can be controlled by the Ir thickness (t_{Ir}) and electric field, thereby providing a good experimental platform for investigating the transition between skyrmion types and the helicity-dependent skyrmion Hall motion. The CoFeB thickness increases from 0.9 to 1.1 nm, and skyrmions are stabilized at room temperature. The $\mathbf{D}_i$ versus t_{Ir} plot is shown in Fig. 3B, showing that $\mathbf{D}_i$ decreases from 0 to −45 μJ/m² as t_{Ir} changes from 0.12 to 0.15 nm. Bloch-type magnetic stripes are present for $-20\ \mu J/m^2 < \mathbf{D}_i < 0$ and that of Néel-type skyrmions for $\mathbf{D}_i < -30\ \mu J/m^2$. The color gradient of the data points in Fig. 3 (B and C) depicts this variation from the Bloch to the Néel state, and the emergent intermediate skyrmion should be located at $\mathbf{D}_i$ of ~−25 μJ/m², for which the skyrmion Hall angle θ_{SKH} is expected to be 0. We note that these $\mathbf{D}_i$ magnitudes are smaller than that in the simulation (T = 0 K) because the experiments are performed at room temperature (300 K). The labels 1 to 4 denote four representative states—(1), (2), (3), and (4)—during this variation, and their Kerr images of SOT-driven motion are shown in Fig. 3C. For state (1): $\mathbf{D}_i$ = 0 (t_{Ir} = 0.12 nm), Bloch stripes (label 1 in Fig. 3, B and C) are stabilized. We note that the formation of Bloch stripes instead of Bloch skyrmions in the experiment is due to a different sequence of experimental procedures from that in the simulation. In the experiment, the Bloch stripes are directly nucleated by applying an external magnetic field. However, in the simulation, a Néel skyrmion is first created, and because of the topological stability, it maintains its shape and thus transforms into a Bloch skyrmion by reducing the iDMI energy. For state (1) in Fig. 3C, the Bloch stripes are perpendicular to the SOT current direction. In this geometry, the Bloch

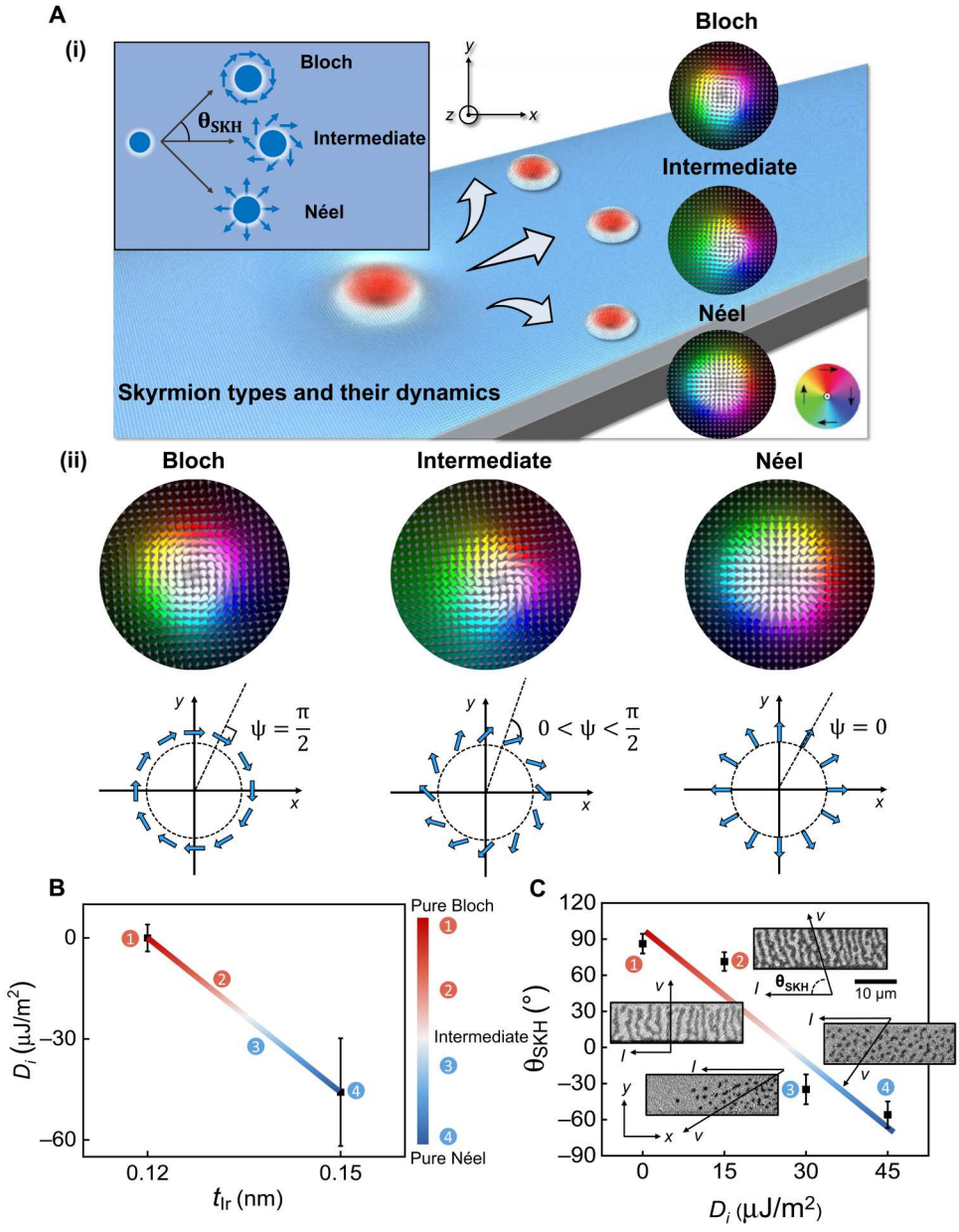

Fig. 3. Dependence of skyrmion motion on topological spin textures. (**A**) Dynamics and spin textures of Bloch, Néel, and intermediate skyrmions. (i) Illustration of the skyrmion Hall effect. The skyrmion Hall (transverse) motion directions or θ_{SKH} of Bloch and Néel skyrmions are opposite. The intermediate skyrmion moves straight with a zero θ_{SKH}. The micromagnetic simulated skyrmion spin textures are shown on the right. The color wheel depicts the spin direction. (ii) Magnified simulated skyrmions and their corresponding spin rotation angles ψ. The intermediate skyrmion is a superposition of the Néel and Bloch skyrmion, with ψ in between. (**B**) $\mathbf{D}_i$ versus Ir thickness. The color depicts the variation of spin texture from pure Bloch to pure Néel type as a function of $\mathbf{D}_i$. Labels 1 to 4 correspond to four states. (**C**) Kerr images of the SOT motion for these four states and their θ_{SKH} versus $\mathbf{D}_i$. Each data point is an average of 50 individual tests. As $\mathbf{D}_i$ decreases, the states change from pure Bloch stripes (state 1) to pure Néel skyrmions (state 4). *I* and *V* are the current and motion directions. Their transverse motion changes from ***+y*** direction (states 1 and 2) to ***−y*** direction (states 3 and 4). State 1, $\theta_{SKH} = +90°$; state 2, $\theta_{SKH} = +70°$; state 3, $\theta_{SKH} = -34°$; state 4, $\theta_{SKH} = -55°$.

stripes move upward perpendicularly to the longitudinal SOT current flow. The velocity and current directions are labeled as *V* and *I*, and the corresponding skyrmion Hall angle is $\theta_{SKH} = +90°$ (the θ_{SKH} measurement technique is discussed in fig. S7). We note that the Bloch DWs in previous sections are parallel to the SOT current direction and hence have zero velocity. This geometry-dependent DW motion was explained by an earlier paper (*40*). For state (2): $\mathbf{D}_i = -15$ μJ/m^2 ($t_{Ir} = 0.13$ nm), as $\mathbf{D}_i$ decreases, the Bloch stripes develop partly to a Néel feature (label 2). They still move upward but with θ_{SKH} decreases to +70° to the current flow. For state (3): $\mathbf{D}_i = -30$ μJ/m^2 ($t_{Ir} = 0.14$ nm), the Bloch stripes transform into Néel skyrmions (label 3). Notably, the transverse motion of these Néel skyrmions is opposite to those Bloch stripes, and now, they move downward with θ_{SKH} decreased to −34°. For state (4): $\mathbf{D}_i$

= −45 μJ/m^2 (t_{Ir} = 0.15 nm), the skyrmions become a pure Néel type, and θ_{SKH} = −55°. From this spin texture–dependent θ_{SKH}, we conclude that the skyrmion type transition and skyrmion Hall effect are correlated to the iDMI chirality and energy.

Next, we investigate the voltage-controlled skyrmion Hall effect. We use the VCDMI to drive the transition between skyrmion types and show that state (3) skyrmion in Fig. 3C can be transformed from Néel to the intermediate skyrmion and then to Bloch type electrically. The detailed characterization of the topological number of this skyrmion is discussed in fig. S8. Figure 4A (i) shows this Néel-type skyrmion motion under zero bias. As described before, the skyrmion moves downward with θ_{SKH} = −34°. A gate bias of +10 V is then applied to transform this skyrmion into the intermediate state with zero θ_{SKH}, and in this case, electric field reduces $\mathbf{D}_i$ to a critical value. As shown in Fig. 4A (ii), the intermediate skyrmions travel almost straight along the $-x$ direction. In Fig. 4A (iii), when the gate bias is further increased to +20 V, the intermediate skyrmion is transformed into a Bloch skyrmion, with a transverse motion in the $+y$ direction. As we can see in Fig. 4A, some skyrmions get elongated (circled by the yellow oval) during their motion due to pinning sites. These elongated skyrmions also serve as another observation of their skyrmion Hall angle (*41*). For example, the elongated Néel skyrmion in Fig. 4A (i) forms a negative angle to the current flow, reflecting its downward ($-y$) transverse motion. In contrast, the elongated Bloch skyrmions in Fig. 4A (iii) form a positive angle to the current flow, reflecting their upward ($+y$) transverse motion. The result of θ_{SKH} is summarized in Fig. 4B: For the Néel skyrmion, θ_{SKH} = −34°; for the intermediate skyrmion, θ_{SKH} = 3°; and for the Bloch skyrmion, θ_{SKH} = 74°. We also perform micromagnetic simulations to corroborate our results. The simulated Néel, intermediate, and Bloch skyrmions are shown in Fig. 3A. As discussed before, the mutual transition between them is enabled by fine-tuning the iDMI energy. The snapshots of their SOT-driven motion are shown in Fig. 4C, and their trajectories are plotted in Fig. 4D. As expected, the Néel and Bloch skyrmions have opposite skyrmion Hall angles, and the intermediate skyrmion moves straight forward along the current direction.

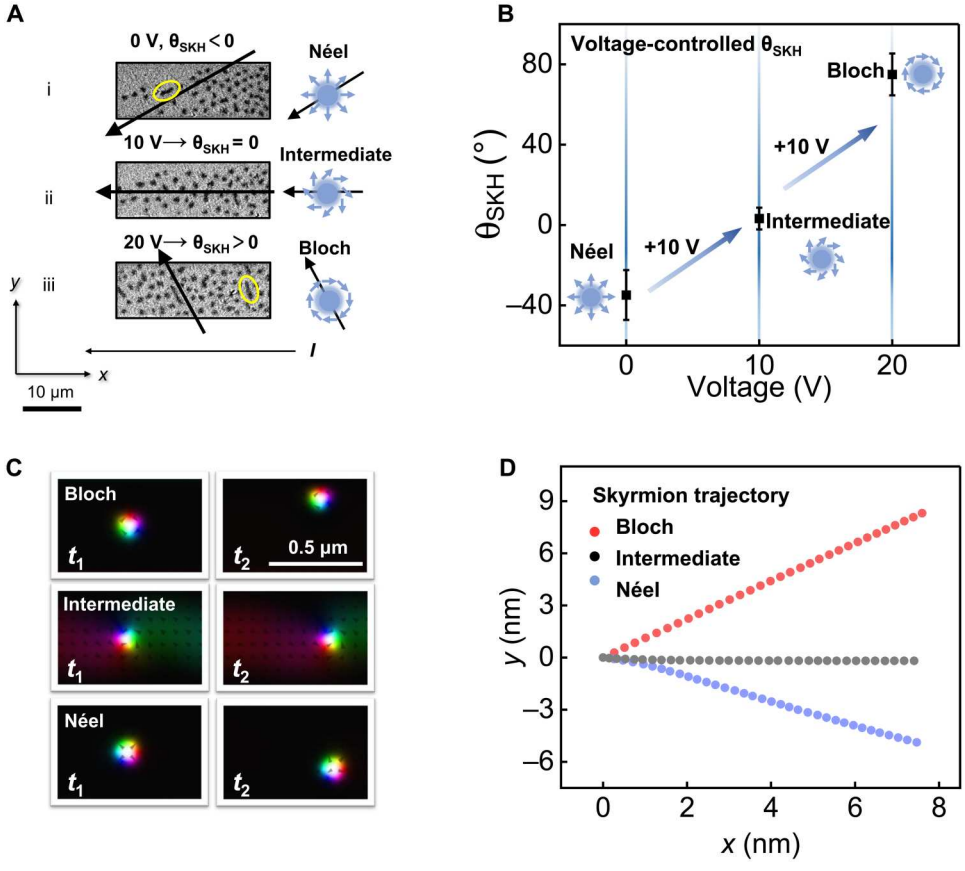

Fig. 4. Voltage control of skyrmion helicity and motion. (**A**) Kerr images demonstrating the voltage-controlled skyrmion types and skyrmion Hall motions. (i) Néel-type skyrmions under 0 V have a $-y$-direction transverse motion. (ii) When +10 V is applied, the Néel skyrmions transform into the intermediate state, showing a straight forward motion along the device. (iii) When +20 V is applied, the intermediate skyrmions transform into Bloch type, having a $+y$-direction transverse motion. The direction of the transverse motion can also be inferred from the elongated skyrmions (circled by yellow ovals). In (A) (i), the elongated skyrmion forms a negative angle to the current flow, indicating a $-y$-direction transverse motion. In (A) (iii), the elongated skyrmions form a positive angle, indicating a $+y$-direction transverse motion. (**B**) θ_{SKH} versus voltage plot. The corresponding θ_{SKH} of the Néel/intermediate/Bloch skyrmions in (A) is measured and quantified. For the Néel skyrmion, θ_{SKH} = −34°; for the intermediate skyrmion, θ_{SKH} = 3°; and for the Bloch skyrmion, θ_{SKH} = 74°. (**C**) Snapshots of micromagnetic simulated SOT-driven skyrmion motion. (**D**) Skyrmion trajectories extracted from (C). Bloch and Néel skyrmions have opposite transverse motion directions, and the intermediate skyrmion moves straight.

DISCUSSION

In conclusion, we have investigated the DMI–electric field interaction of magnetic heterostructures and achieved the voltage-driven DMI chirality transition. Using this VCDMI effect, the skyrmion types along with their helicity-dependent skyrmion Hall effect can be controlled, and a type of intermediate skyrmion with a straight motion has been created. Our work demonstrates the understanding of the atomic-scale DMI–electric field interaction that affects spin chirality, skyrmion helicity, and skyrmion dynamics. It provides a platform for investigating chiral exchange interactions at the atomic interface and their effect on the skyrmion dynamics. Our work will attract and promote general interest in the emerging field of voltage-controlled chiral interactions and voltage-controlled skyrmionics.

MATERIALS AND METHODS

Layers consisting of Ta(5)/CoFeB(0.9 and 1.1)/Ir(0.03 to 0.15)/MgO(2)/Al_2O_3(5) were grown on Si/SiO_2 substrates by dc and radiofrequency magnetron sputtering at room temperature (numbers in parentheses represent thickness in nanometers). The Ir layer has a wedge shape with a continuously changing thickness with a nominal gradient of 0.02 nm/1 cm of the sample length. The samples were then patterned into an array of top-gate DW motion racetrack devices using standard photolithography techniques. A 60-nm Al_2O_3 gate dielectric was deposited using atomic layer deposition, and a 90-nm indium tin oxide layer was fabricated as the transparent top-gate electrode. The dimensions of the devices are 100 μm by 5 μm and 100 μm by 10 μm.

The polar magneto-optic Kerr effect (MOKE) imaging experiments were carried out using a spatially (360-nm resolution) and temporally (20-ms resolution) resolved polar MOKE microscope. The external magnetic field was generated by a Helmholtz coil driven by a Kepco power supply. The current pulses were applied using a Keithley 2612A source-meter, and the dc top-gate voltages were applied using a Keithley 2400 source-meter. All measurements were carried out at room temperature.

Micromagnetic simulations were performed using the MuMax3 software (*39*). The systems were modeled using a cell size of 4 nm by 4 nm by 1.1 nm with a grid size of 1024 by 128 by 1, yielding a world size of 4096 nm by 512 nm by 1.1 nm. The simulations used a saturation magnetization of 9×10^5 A/m, an exchange constant of 1.0×10^{-11} J/m, and an out-of-plane uniaxial anisotropy of 5×10^5 J/m^3. The system was initialized into a uniformly magnetized state in the z directions. The Néel skyrmion was stabilized by an iDMI of 500 μJ/m^2 and a magnetic field of 0.02 T. It was transformed into an intermediate skyrmion by reducing the iDMI to 200 μJ/m^2 and magnetic field to 0.01 T. The intermediate skyrmion was transformed into a Bloch skyrmion by reducing the iDMI to 0 μJ/m^2 and maintaining the same magnetic field of 0.01 T. The motion of these three types of skyrmion was driven by a SOT current with a spin Hall angle of 0.3. The details of the implementation of the simulation solvers and methods can be found in (*39*).

Supplementary Materials

This PDF file includes:

Supplementary Text
Figs. S1 to S8
Table S1
References

REFERENCES AND NOTES

1. I. Dzyaloshinsky, A thermodynamic theory of "weak" ferromagnetism of antiferromagnetics. *J. Phys. Chem. Solid* **4**, 241–255 (1958).
2. T. Moriya, Anisotropic superexchange interaction and weak ferromagnetism. *Phys. Rev.* **120**, 91–98 (1960).
3. X. Z. Yu, Y. Onose, N. Kanazawa, J. H. Park, J. H. Han, Y. Matsui, N. Nagaosa, Y. Tokura, Real-space observation of a two-dimensional skyrmion crystal. *Nature* **465**, 901–904 (2010).
4. A. Neubauer, C. Pfleiderer, B. Binz, A. Rosch, R. Ritz, P. G. Niklowitz, P. Böni, Topological Hall effect in the a phase of MnSi. *Phys. Rev. Lett.* **102**, 186602 (2009).
5. A. K. Nayak, V. Kumar, T. Ma, P. Werner, E. Pippel, R. Sahoo, F. Damay, U. K. Rößler, C. Felser, S. S. P. Parkin, Magnetic antiskyrmions above room temperature in tetragonal Heusler materials. *Nature* **548**, 561–566 (2017).
6. X. Ma, G. Q. Yu, C. Tang, X. Li, C. L. He, J. Shi, K. L. Wang, X. Q. Li, Interfacial Dzyaloshinskii-Moriya interaction: Effect of 5*d* band filling and correlation with spin mixing conductance. *Phys. Rev. Lett.* **120**, 157204 (2018).
7. A. Soumyanarayanan, M. Raju, A. L. G. Oyarce, A. K. C. Tan, M.-Y. Im, A. P. Petrović, P. Ho, K. H. Khoo, M. Tran, C. K. Gan, F. Ernult, C. Panagopoulos, Tunable room-temperature magnetic skyrmions in Ir/Fe/Co/Pt multilayers. *Nat. Mater.* **16**, 898–904 (2017).
8. A. Fert, P. M. Levy, Role of anisotropic exchange interactions in determining the properties of spin-glasses. *Phys. Rev. Lett.* **44**, 1538–1541 (1980).
9. W. Jiang, P. Upadhyaya, W. Zhang, G. Yu, M. B. Jungfleisch, F. Y. Fradin, J. E. Pearson, Y. Tserkovnyak, K. L. Wang, O. Heinonen, S. G. E. te Velthuis, A. Hoffmann, Blowing magnetic skyrmion bubbles. *Science* **349**, 283–286 (2015).
10. G. Yu, P. Upadhyaya, X. Li, W. Li, S. K. Kim, Y. Fan, K. L. Wong, Y. Tserkovnyak, P. K. Amiri, K. L. Wang, Room-temperature creation and spin-orbit torque manipulation of skyrmions in thin films with engineered asymmetry. *Nano Lett.* **16**, 1981–1988 (2016).
11. K.-S. Ryu, L. Thomas, S.-H. Yang, S. Parkin, Chiral spin torque at magnetic domain walls. *Nat. Nanotechnol.* **8**, 527–533 (2013).
12. S. Emori, U. Bauer, S.-M. Ahn, E. Martinez, G. S. Beach, Current-driven dynamics of chiral ferromagnetic domain walls. *Nat. Mater.* **12**, 611–616 (2013).
13. G. Yu, P. Upadhyaya, Q. Shao, H. Wu, G. Yin, X. Li, C. He, W. Jiang, X. Han, P. K. Amiri, K. L. Wang, Room-temperature skyrmion shift device for memory application. *Nano Lett.* **17**, 261–268 (2017).
14. S. S. P. Parkin, M. Hayashi, L. Thomas, Magnetic domain-wall racetrack memory. *Science* **320**, 190–194 (2008).
15. K. M. Song, J.-S. Jeong, B. Pan, X. Zhang, J. Xia, S. Cha, T.-E. Park, K. Kim, S. Finizio, J. Raabe, J. Chang, Y. Zhou, W. Zhao, W. Kang, H. Ju, S. Woo, Skyrmion-based artificial synapses for neuromorphic computing. *Nat. Electron.* **3**, 148–155 (2020).
16. C. O. Avci, E. Rosenberg, L. Caretta, F. Büttner, M. Mann, C. Marcus, D. Bono, C. A. Ross, G. S. D. Beach, Interface-driven chiral magnetism and current-driven domain walls in insulating magnetic garnets. *Nat. Nanotechnol.* **14**, 561–566 (2019).
17. H. Wu, F. Groß, B. Dai, D. Lujan, S. A. Razavi, P. Zhang, Y. Liu, K. Sobotkiewich, J. Förster, M. Weigand, G. Schütz, X. Li, J. Gräfe, K. L. Wang, Ferrimagnetic skyrmions in topological insulator/ferrimagnet heterostructures. *Adv. Mater.* **32**, 2003380 (2020).
18. L. Caretta, S.-H. Oh, T. Fakhrul, D.-K. Lee, B. H. Lee, S. K. Kim, C. A. Ross, K.-J. Lee, G. S. D. Beach, Relativistic kinematics of a magnetic soliton. *Science* **370**, 1438–1442 (2020).
19. L. Caretta, M. Mann, F. Büttner, K. Ueda, B. Pfau, C. M. Günther, P. Hessing, A. Churikova, C. Klose, M. Schneider, D. Engel, C. Marcus, D. Bono, K. Bagschik, S. Eisebitt, G. S. D. Beach, Fast current-driven domain walls and small skyrmions in a compensated ferrimagnet. *Nat. Nanotechnol.* **13**, 1154–1160 (2018).
20. N. Romming, A. Kubetzka, C. Hanneken, K. von Bergmann, R. Wiesendanger, Field-dependent size and shape of single magnetic skyrmions. *Phys. Rev. Lett.* **114**, 177203 (2015).
21. F. Büttner, I. Lemesh, G. S. D. Beach, Theory of isolated magnetic skyrmions: From fundamentals to room temperature applications. *Sci. Rep.* **8**, 4464 (2018).
22. P. F. Bessarab, G. P. Müller, I. S. Lobanov, F. N. Rybakov, N. S. Kiselev, H. Jónsson, V. M. Uzdin, S. Blügel, L. Bergqvist, A. Delin, Lifetime of racetrack skyrmions. *Sci. Rep.* **8**, 3433 (2018).
23. G. Chen, A. Mascaraque, H. Y. Jia, B. Zimmermann, M. Robertson, R. Lo Conte, M. Hoffmann, M. A. G. Barrio, H. F. Ding, R. Wiesendanger, E. G. Michel, S. Blügel, A. K. Schmid, K. Liu, Large Dzyaloshinskii-Moriya interaction induced by chemisorbed oxygen on a ferromagnet surface. *Sci. Adv.* **6**, eaba4924 (2020).
24. G. Chen, M. Robertson, M. Hoffmann, C. Ophus, A. L. Fernandes Cauduro, R. lo Conte, H. Ding, R. Wiesendanger, S. Blügel, A. K. Schmid, K. Liu, Observation of hydrogen-induced

Dzyaloshinskii-Moriya interaction and reversible switching of magnetic chirality. *Phys. Rev. X* **11**, 021015 (2021).
25. T. Srivastava, M. Schott, R. Juge, V. Křižáková, M. Belmeguenai, Y. Roussigné, A. Bernand-Mantel, L. Ranno, S. Pizzini, S. M. Chérif, A. Stashkevich, S. Auffret, O. Boulle, G. Gaudin, M. Chshiev, C. Baraduc, H. Béa, Large-voltage tuning of Dzyaloshinskii-Moriya interactions: A route toward dynamic control of skyrmion chirality. *Nano Lett.* **18**, 4871–4877 (2018).
26. T. Koyama, Y. Nakatani, J. I. Ieda, D. Chiba, Electric field control of magnetic domain wall motion via modulation of the Dzyaloshinskii-Moriya interaction. *Sci. Adv.* **4**, eaav0265 (2018).
27. T. Maruyama, Y. Shiota, T. Nozaki, K. Ohta, N. Toda, M. Mizuguchi, A. A. Tulapurkar, T. Shinjo, M. Shiraishi, S. Mizukami, Y. Ando, Y. Suzuki, Large voltage-induced magnetic anisotropy change in a few atomic layers of iron. *Nat. Nanotechnol.* **4**, 158–161 (2009).
28. X. Li, K. Fitzell, D. Wu, C. T. Karaba, A. Buditama, G. Yu, K. L. Wong, N. Altieri, C. Grezes, N. Kioussis, S. Tolbert, Z. Zhang, J. P. Chang, P. Khalili Amiri, K. L. Wang, Enhancement of voltage-controlled magnetic anisotropy through precise control of Mg insertion thickness at CoFeB|MgO interface. *Appl. Phys. Lett.* **110**, 052401 (2017).
29. C. Grezes, F. Ebrahimi, J. G. Alzate, X. Cai, J. A. Katine, J. Langer, B. Ocker, P. Khalili Amiri, K. L. Wang, Ultra-low switching energy and scaling in electric-field-controlled nanoscale magnetic tunnel junctions with high resistance-area product. *Appl. Phys. Lett.* **108**, 012403 (2016).
30. S. Emori, E. Martinez, K.-J. Lee, H.-W. Lee, U. Bauer, S.-M. Ahn, P. Agrawal, D. C. Bono, G. S. D. Beach, Spin Hall torque magnetometry of Dzyaloshinskii domain walls. *Phys. Rev. B* **90**, 184427 (2014).
31. L. Caretta, E. Rosenberg, F. Büttner, T. Fakhrul, P. Gargiani, M. Valvidares, Z. Chen, P. Reddy, D. A. Muller, C. A. Ross, G. S. D. Beach, Interfacial Dzyaloshinskii-Moriya interaction arising from rare-earth orbital magnetism in insulating magnetic oxides. *Nat. Commun.* **11**, 1090 (2020).
32. L. Liu, C. F. Pai, Y. Li, H. W. Tseng, D. C. Ralph, R. A. Buhrman, Spin-torque switching with the giant spin Hall effect of tantalum. *Science* **336**, 555–558 (2012).
33. A. Belabbes, G. Bihlmayer, F. Bechstedt, S. Blügel, A. Manchon, Hund's rule-driven Dzyaloshinskii-Moriya interaction at 3*d*-5*d* interfaces. *Phys. Rev. Lett.* **117**, 247202 (2016).
34. V. Kashid, T. Schena, B. Zimmermann, Y. Mokrousov, S. Blügel, V. Shah, H. G. Salunke, Dzyaloshinskii-Moriya interaction and chiral magnetism in 3*d*–5*d* zigzag chains: Tight-binding model and ab initio calculations. *Phys. Rev. B* **90**, 054412 (2014).
35. S. Miwa, M. Suzuki, M. Tsujikawa, K. Matsuda, T. Nozaki, K. Tanaka, T. Tsukahara, K. Nawaoka, M. Goto, Y. Kotani, T. Ohkubo, F. Bonell, E. Tamura, K. Hono, T. Nakamura, M. Shirai, S. Yuasa, Y. Suzuki, Voltage controlled interfacial magnetism through platinum orbits. *Nat. Commun.* **8**, 15848 (2017).
36. H. Vakili, Y. Xie, A. W. Ghosh, Self-focusing hybrid skyrmions in spatially varying canted ferromagnetic systems. *Phys. Rev. B* **102**, 174420 (2020).
37. W. Jiang, X. Zhang, G. Yu, W. Zhang, X. Wang, M. Benjamin Jungfleisch, J. E. Pearson, X. Cheng, O. Heinonen, K. L. Wang, Y. Zhou, A. Hoffmann, S. G. E. Te Velthuis, Direct observation of the skyrmion Hall effect. *Nat. Phys.* **13**, 162–169 (2017).
38. K. Litzius, I. Lemesh, B. Krüger, P. Bassirian, L. Caretta, K. Richter, F. Büttner, K. Sato, O. A. Tretiakov, J. Förster, R. M. Reeve, M. Weigand, I. Bykova, H. Stoll, G. Schütz, G. S. D. Beach, M. Klaüi, Skyrmion Hall effect revealed by direct time-resolved x-ray microscopy. *Nat. Phys.* **13**, 170–175 (2017).
39. A. Vansteenkiste, J. Leliaert, M. Dvornik, M. Helsen, F. Garcia-Sanchez, B. van Waeyenberge, The design and verification of MuMax3. *AIP Adv.* **4**, 107133 (2014).
40. A. V. Khvalkovskiy, V. Cros, D. Apalkov, V. Nikitin, M. Krounbi, K. A. Zvezdin, A. Anane, J. Grollier, A. Fert, Matching domain-wall configuration and spin-orbit torques for efficient domain-wall motion. *Phys. Rev. B* **87**, 020402(R) (2013).
41. Y. Hirata, D.-H. Kim, S. K. Kim, D.-K. Lee, S.-H. Oh, D.-Y. Kim, T. Nishimura, T. Okuno, Y. Futakawa, H. Yoshikawa, A. Tsukamoto, Y. Tserkovnyak, Y. Shiota, T. Moriyama, S. B. Choe, K.-J. Lee, T. Ono, Vanishing skyrmion Hall effect at the angular momentum compensation temperature of a ferrimagnet. *Nat. Nanotechnol.* **14**, 232–236 (2019).
42. G. Kresse, J. Furthmüller, Efficient iterative schemes for ab initio total-energy calculations using a plane-wave basis set. *Phys. Rev. B Condens. Matter* **54**, 11169–11186 (1996).
43. G. Kresse, J. Furthmüller, Efficiency of ab-initio total energy calculations for metals and semiconductors using a plane-wave basis set. *Comput. Mater. Sci.* **6**, 15–50 (1996).
44. J. P. Perdew, K. Burke, M. Ernzerhof, Generalized gradient approximation made simple. *Phys. Rev. Lett.* **77**, 3865–3868 (1996).
45. G. Kresse, D. Joubert, From ultrasoft pseudopotentials to the projector augmented-wave method. *Phys. Rev. B* **59**, 1758–1775 (1999).
46. P. E. Blöchl, Projector augmented-wave method. *Phys. Rev. B* **50**, 17953–17979 (1994).
47. F. Mahfouzi, N. Kioussis, First-principles calculation of the Dzyaloshinskii-Moriya interaction: A Green's function approach. *Phys. Rev. B* **103**, 094410 (2021).
48. T. Ozaki, Variationally optimized atomic orbitals for large-scale electronic structures. *Phys. Rev. B* **67**, 155108 (2003).
49. T. Ozaki, H. Kino, Numerical atomic basis orbitals from H to Kr. *Phys. Rev. B* **69**, 195113 (2004).
50. T. Ozaki, H. Kino, Efficient projector expansion for the ab initio LCAO method. *Phys. Rev. B* **72**, 045121 (2005).

Acknowledgments

Funding: We acknowledge the support from the National Science Foundation (NSF) award nos. 1411085, 1810163, 1935362, 1909416, 1810163, and 1611570; the Nanosystems Engineering Research Center for Translational Applications of Nanoscale Multiferroic Systems (TANMS); the Intel Corporation under contract no. 52318957; and the Army Research Office Multidisciplinary University Research Initiative (MURI) under grant nos. W911NF16-1-0472 and W911NF-19-S-0008. **Author contributions:** B.D. and K.L.W. conceived and designed the experiments. K.L.W. supervised the work. B.D., D.W., and S.A.R. grew the samples. K.W. fabricated the devices. B.D. carried out the optical and transport experiments. F.M. and N.K. performed the first-principles calculations. B.D. processed the data. All authors contributed to the analyses. B.D. and K.L.W. wrote the manuscript with contributions from all authors. **Competing interests:** The authors declare that they have no competing interests. **Data and materials availability:** All data needed to evaluate the conclusions in the paper are present in the paper and/or the Supplementary Materials.

Submitted 31 August 2022
Accepted 12 January 2023
Published 15 February 2023
10.1126/sciadv.ade6836